Automatic Liver Segmentation based on Shape Constraints and Deformable Graph Cut in CT Images

Guodong Li #, Xinjian Chen #, Fei Shi, Weifang Zhu, Jie Tian*, *Fellow, IEEE*, Dehui Xiang*

Abstract—Liver segmentation is still a challenging task in medical image processing area due to the complexity of the liver's anatomy, low contrast with adjacent organs and presence of pathologies. This investigation was used to develop and validate an automated method to segment livers in CT images. The proposed framework consists of three steps: preprocessing, initialization and segmentation. In the first step, statistical shape model is constructed based on principal component analysis and the input image is smoothed using curvature anisotropic diffusion filtering. In the second step, the mean shape model is moved by using thresholding and Euclidean distance transformation to obtain a coarse position in a test image, and then the initial mesh is locally and iteratively deformed to the coarse boundary, which is constrained to stay close to a subspace of shapes describing the anatomical variability. Finally, in order to accurately detect the liver surface, deformable graph cut was proposed, which effectively integrates the properties and inter-relationship of the input images and initialized surface. The proposed method was evaluated on 50 CT scan images, which are publicly available in two databases Sliver07 and 3Dircadb. The experimental results showed that the proposed method was effective and accurate for detection of the liver surface.

Index Terms—Liver Segmentation, Principal Component Analysis, Euclidean Distance Transformation, Deformable Graph Cut.

I. INTRODUCTION

L IVER cancer has been among the 6 most common cancers and also a leading cause of cancer deaths worldwide. In 2012, it was reported that about 782,000 new cases were diagnosed with liver cancer and about 745, 000 people died from this disease worldwide [1]. Consequently, particular effort is being made in early diagnosis and therapy. Liver segmentation in medical images is very important to accurately evaluate patient-specific liver anatomy for hepatic disease diagnosis, function assessment and treatment decision-making. Computed Tomography (CT) is now well-established for noninvasive diagnosis of hepatic disease due to recent
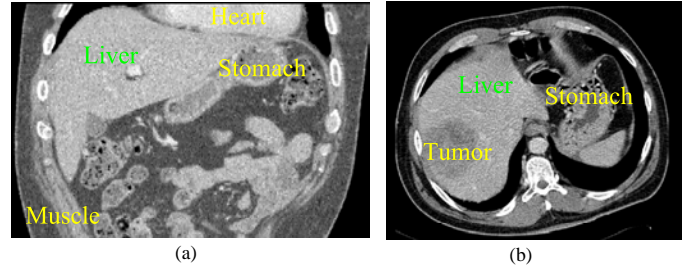
Fig. 1. Examples of the complex anatomical structures and large variations of liver shapes. (a) A CT image slice of a healthy person in coronal view. (b) A CT image slice in axial view from one patient with liver cancer. The normal liver and its several neighboring organs share similar intensities while the liver parenchyma and pathological changes exhibit non-homogeneous gray level.

technological advances in X-ray tubes, detectors, and reconstruction algorithms. On the other hand, the amount of data produced by high resolution CT scanners, as well as the time needed to review the resulting several thousand slices, has been continuously increasing, which makes it tedious and time-consuming for radiologists and physicians [2]. Semi-automatic or automatic liver segmentation are helpful and advisable in clinical applications. Recently, numerous methods have been proposed to segment livers effectively and efficiently. Many researchers have provided publicly available datasets and/or organized liver segmentation competitions to investigate those current segmentation algorithms [3].

Although CT images have been widely used in clinics, liver segmentation is still a challenging task in the medical image processing field. As can be seen in Fig.1, there are several special characteristics from the liver's anatomical structure. First, there are several neighboring organs, e.g. muscles, heart and stomach, and they share similar intensities, which lead to low contrast and blurred boundaries in CT images between the liver and its neighboring organs. Therefore, liver segmentation using pixel based methods such as region growing may easily leak to neighboring organs. Second, image artifacts, noise and various pathologies, such as tumors often exist. Liver segmentation can be disturbed by different gray value intervals between hepatic tissues and artifacts. To tackle these problems, shape priors are desirable and advisable, since they can help to separate adjacent organs with similar intensities and preserve liver shape with non-homogeneous gray level [4]. However, liver shape modeling is not a trivial task. Anatomy of the liver varies largely from different health individuals both in

shape and size. Besides, tumors and other pathologies may also change anatomical structure of a liver.

In this paper, we introduce a coarse-to-fine approach for the segmentation of the whole liver from CT images. To make the method automatic, the liver first needs to be localized in the image. This task is challenging due to inter-patient and inter-phase shape variability, liver pose and location variability in the abdomen, variation in reconstructed field-of-view (the reconstructed image may focus on the liver or may cover the whole chest and abdomen). After successful liver initialization using model adaptation method, liver shape can be adapted to the coarse boundary. Due to the complexity of liver anatomy, influenced by adjacent organs and insufficiency of shape *prior*, it makes accurate segmentation difficult. The patient's anatomy is accurately and more robustly segmented using the proposed deformable graph cut in a narrow band, which is well suited for inter-patient and inter-phase shape variability. The proposed deformable graph cut can reduce under-segmentation or over-segmentation of livers since shape constraints are integrated into region cost and boundary cost of the traditional graph cut [5]–[7] in a narrow band of the initial shape.

II. RELATED WORK

In the last few decades, many approaches have been proposed for liver segmentation. A comprehensive review of different methods have been presented [3], [8]. Simple pixel-based methods [9]–[12] include global thresholding, region growing, voxel classification, or edge detection. Zhou *et al.* [9] used a probabilistic model to estimate the initial spatial location and calculated the liver probability to automatically segment the liver from non-contrast X-ray Torso CT images. van Rikxoort *et al.* [10] estimated the probability that each voxel is part of the liver using a k-nearest-neighbor classifier and a multi-atlas registration procedure to automatically delineate the liver from CT images. Foruzan *et al.* [12] proposed an intensity analysis and anatomical information based method. The authors used an expectation maximization (EM) algorithm to compute statistical parameters of the liver's intensity range, and combined a thresholding approach and an anatomical based rule to interactively differentiate the liver from its surrounding tissues. The region-growing based liver segmentation approaches [11], [13], [14] can obtain good results from contrast enhanced CT images but they are very sensitive to initial seeds. Overall, pixel-based methods can usually fail to automatically segment a liver due to noise, similar gray-value distribution with neighboring organs, etc.

In 1993, Cootes *et al.* [15] introduced active shape models to image segmentation. Typically, 3D point distribution model (PDM) based statistical shape models (SSMs) were used in [16]–[18] to automatically segment the liver from CT images. These approaches first build a statistical model from a training set of liver shapes. Each liver shape is represented by some corresponding landmarks sampled on the surface in the training stage. Lamecker *et al.* [16] applied a SSM based method with grey value profile model to segment livers. Kainmüller *et al.* [17] integrated SSMs to a free-form segmentation method. Zhang *et al.* [18] obtained a coarse liver shapes in

a test CT images using a generalized Hough transformation based subspace initialization method, and then detected liver boundaries using optimal surface segmentation. The optimal surface detection algorithm proposed by Li *et al.* [19] was used to find a minimum-cost closed set in a vertex-weighted graph using max-flow/min-cut algorithms [6]. Heimann and Meinzer [3] presented an overview of SSMs based methods for segmentation of medical images. Wang *et al.* [4] integrated a sparse shape composition model and a fast marching level set method to achieve accurate segmentation of the hepatic parenchyma, portal veins, hepatic veins, and tumors simultaneously. Subsequently, they employed a homotopy-based method to solve the L1-norm optimization problem [20].

Graph cut was employed to segment liver automatically since it was introduced by Boykov *et al.* [5]–[7]. To deal with the intense memory requirements and the supralinear time complexity for traditional graph cut, Lombaert *et al.* [21] introduced a multilevel banded graph cuts method for fast image segmentation. Xe *et al.* [22] used a graph cuts based active contour method for image segmentation in a narrow band. Massoptier *et al.* [23] applied a graph-cut method initialized by an adaptive threshold to perform fully automatic liver segmentation in CT images. Beichel *et al.* [24] developed an interactive segmentation system which allowed the user to manipulate liver volume by combining a graph cuts segmentation method and a three-dimensional virtual reality based segmentation refinement approach. Linguraru *et al.* [25] employed a 3-D affine invariant shape parameterization method to compare features of a set of closed 3-D surfaces point-to-point correspondence to detect shape ambiguities on an initial segmentation of the liver and used a shape-driven geodesic active contour method to segment the liver, followed by hepatic tumor segmentation using graph cut. Chen *et al.* [26] combined an oriented active appearance model with a pseudo-3-D initialization strategy and shape constrained graph cuts to automatically segment livers. Song *et al.* [27] roughly segmented the liver based on a kernel fuzzy C-means algorithm with spatial information and the refined segmentation was performed based on the GrowCut algorithm. Tomoshige *et al.* [28] combined a level set based conditional statistical shape model and graph cuts segmentation based on the estimated shape *prior* to automatic liver segmentation from non-contrast abdominal CT volumes.

As described above, SSM based methods are desirable and helpful to automatically segment livers from complex CT images. Such methods use landmarks to represent shape and describe shape variation in the training data sets, which are difficult to account for in a specific target organ. Graph-based methods can be utilized to search for a global optimal solution while foreground seeds and background seeds are often needed traditionally. Therefore, our aim is to combine the complementary strengths of these methods to automatically and robustly segment livers from CT images in this paper. Compared to previous graph cut methods [5]–[7], [21], [26], [28], the contributions of our method are as follows,

- Model initialization is performed by the integration of principal component analysis (PCA), Euclidean distance transformation (EDT) and deformable adaptation of the
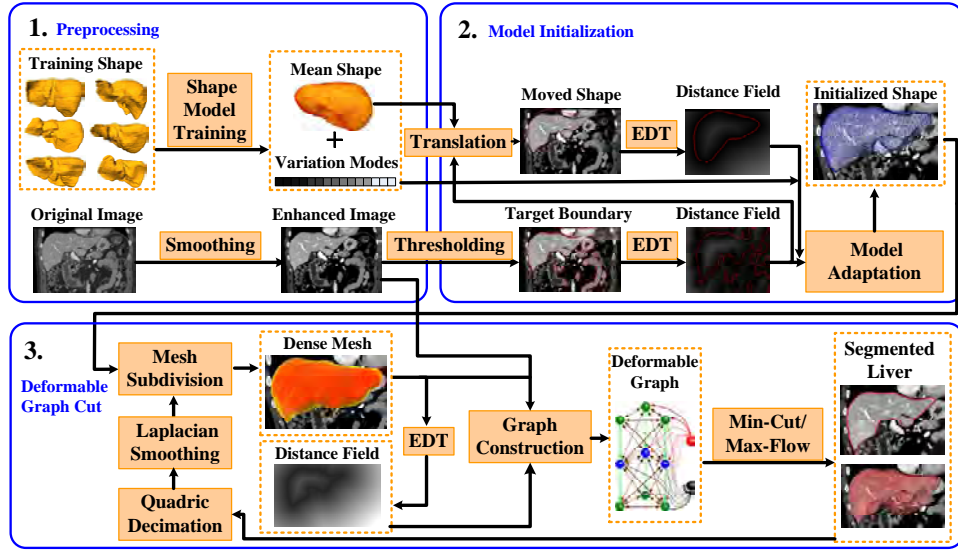
Fig. 2. The proposed segmentation framework. In the preprocessing step, shape models are trained for localization and segmentation, and original images are smoothed. In the initialization step, the initial liver surface is detected using model adaptation. In the segmentation step, accurate liver surface detection is achieved by the proposed deformable graph cut.

liver shape model. We show that the fast EDT based method is able to detect the liver despite hepatic shape and pose variability and for different imaging protocols. This model adaptation process can be described as minimizing the distance between the deformed mesh and the coarse boundary, which is based on region and surface constraints.

- Inspired by [18], [19], [29], [30], a new graph is constructed to achieve an accurate liver surface detection by using the proposed deformable graph cut. Compared to traditional graph cut, the novelties of the proposed graph lie in arcs and weights. Compared to graph search, it can integrate shape *prior* and different weights. The presented approach can reduce under-segmentation or over-segmentation of livers.

In the rest of this paper, in Section III, the complete methodology of the segmentation algorithm is outlined. In Section IV, preprocessing is described to construct a mean liver shape model and smooth input CT volume. Section V introduces the encoding of *prior* knowledge into liver models to initialize segmentation. In Section VI, a final segmentation method is presented. In Section VII, we describe an evaluation of this method in terms of its accuracy and efficiency. In Section VIII, we summarize our contributions and conclusions.

III. METHOD OVERVIEW

The proposed method is a coarse to fine segmentation approach which consists of three major steps: 1) preprocessing, 2) model initialization, and 3) accurate surface detection. Fig. 2 shows the framework of the proposed method. In the preprocessing step, the mean shape model and its variation modes are computed using PCA after training livers are manually segmented, corresponded and aligned. For a test image, it is smoothed through curvature anisotropic diffusion filtering. In the initialization step, the mean shape model
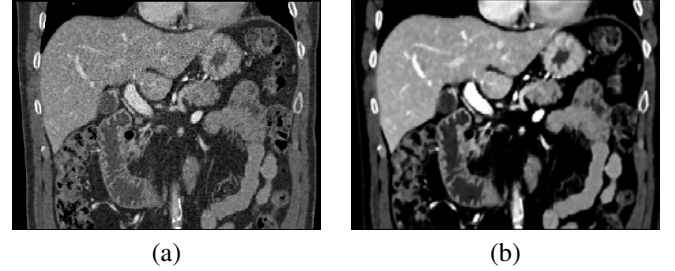

Fig. 3. Image Enhancement. (a) Original image. (b) Enhanced image using curvature anisotropic diffusion filtering.

is translated according to a thresholded image and signed Euclidean distance field of the test image. The moved mean shape model is deformed based on its PDM and driven to the target boundary. To accurately detect the boundary of a liver, the deformable graph cut is presented to progressively find the optimal surface with a minimal cost. The proposed deformable graph cut effectively integrates shape information with optimal 3-D delineation capability of graph cut method.

IV. IMAGE PREPROCESSING

Before the initialization, an image preprocessing procedure is applied to construct mean liver shape models and smooth input CT volume. The mean liver shape model is trained by using PCA, and CT images are enhanced by applying a curvature anisotropic diffusion filter [31], as shown in Fig.3.

Statistical information can be learned from manually annotated images. These training images should be collected from clinical applications and should reflect the variability of the target object, such that the segmentation algorithm can be applicable to the clinical question. However, adapting two uncalibrated meshes with some motions such as significant rotation and scale changes still remains a difficult problem. The labeled binary images are converted into triangulated

meshes to represent manual segmentation by using the marching cube algorithm [32]. In order to reduce the time complexity of the correspondence construction algorithm, all meshes are simplified by using the quadric error metric algorithm [33] with the same $\mathcal{V}$ vertices connected in $\mathcal{T}$ triangles. The minimum description length (MDL) algorithm [34] is then used to establish vertex correspondence between the reference meshes. After obtaining the corresponding relationship between all reference meshes for the training data, surfaces need to be aligned in one Cartesian coordinate system by similarity transformation, in order to analyze inter-patient and inter-phase shape variability. One point set of a mesh in the training data set is randomly selected as a reference point set, the rest of the point sets are considered as a floating point data set, and the alignment is done by similarity transformation in the three-dimensional space using the unit quaternion algorithm [35].

The PDM can be used to describe shape variability using PCA. With the combination of similarity transformation, the resulting PDM can be expressed as

$$\Psi_k = T^{-1}\left(\bar{\Psi} + \sum_{m=1}^{M} \lambda_{m,k} p_m\right) \qquad (1)$$

where, Ψ_k denotes the kth triangulated mesh aligned using similarity transformation from manual segmentation in the training set ($k = 1, 2, \cdots, n_f$), n_f is the number of manual segmented liver. T^{-1} is the inverse of similarity transformation from the registered shape coordinate system to the original coordinate system and $\bar{\Psi}$ is the mean shape of the training set. p_m is the principal mode of variation obtained through PCA. $\lambda_{m,k}$ is the corresponding weight for each principal mode. M is the number of modes. The mean shape model is computed by

$$\bar{\Psi} = \frac{1}{n_f} \sum_{k=1}^{n_f} \Psi_k \qquad (2)$$

V. MODEL INITIALIZATION

Acting as an important role in our method, model initialization provides a coarse surface for the deformable graph cut and makes our approach automatic. A shape *prior* can be learned from a representative set of generated meshes from training images. The derived information can then be associated to the vertices to improve and constrain the initialization. The initialization algorithm proposed in this paper preserves the mesh correspondence during adaptation (i.e., no vertex or triangle is removed or inserted).

After input images are enhanced using curvature anisotropic diffusion filtering, the initial position of the target liver should be computed. The rough contour of the target liver which may couple with several disjointed non-liver regions, can be identified by thresholding. A small threshold value, e.g. 5% of the maximal intensity value, can be enough. Since some adjacent tissues are similar to the liver, morphological opening can be used to remove those small structures. On the other hand, hepatic lobes may be delineated in some slices, and then morphological closing can be applied to connect the disjointed regions or fill holes. In the experiments, we could
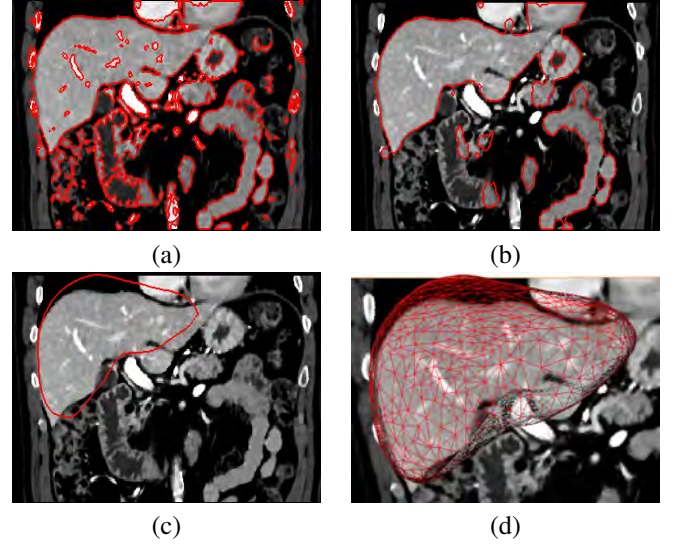

Fig. 4. Shape model location. (a) An enhanced image with a thresholded image (red curve); (b) An enhanced image with a processed image (red curve) with morphological operations; (c) Moved shape model in 2D slice view; (d) Moved shape model in 3D slice view.

observe that position computation was not very sensitive to those exact threshold values or radii of structuring elements for morphological operations and can be successfully employed. The distance transformation is then performed in the binary images. The algorithm computes Euclidean distance for d-dimensional images in linear time [36]. This algorithm is time efficient and the results are sufficient for center computation. The signed Euclidean distance field can be considered as $\Gamma_t(p)$, p denotes the image voxel, t is the segmented surface obtained from the binary image I_b by using the marching cube algorithm [32]. The initial position can be estimated with minimal Euclidean distance as the Step 1 in Algorithm 1.

In order to adapt a mesh to the liver boundary in a testing image, shape-constrained deformable models were used and a PDM was also integrated into the deformable model framework [2]. The initial mesh is locally deformed to the boundary, which is constrained to stay close to a subspace of shapes describing the anatomical variability. In this procedure, the initial mesh is adapted to the target boundary and the initial image is matched to the thresholded image in two alternating steps. In each iteration, the first step consists of mesh deformation by progressively detecting the candidate boundary along the normal of vertices such that the deformed mesh Ψ_τ can be driven to the boundary. In the second step, the parameters of the mean shape are adjusted to generate a subspace shape model Ψ_λ and constrains the deformation of Ψ_τ (initially the moved mean shape). This optimization process can be described as minimizing the distance E between the deformed mesh and the boundary. The objective function can be defined as,

$$E = E_{region} + \kappa E_{surface} \qquad (3)$$

where, E_{region} denotes a region term, which measures the distance between Ψ_τ and Ψ_t in the signed Euclidean distance field; Ψ_t represents mesh of the thresholded image; p represents a voxel in Euclidean distance field Γ; $E_{surface}$ denotes
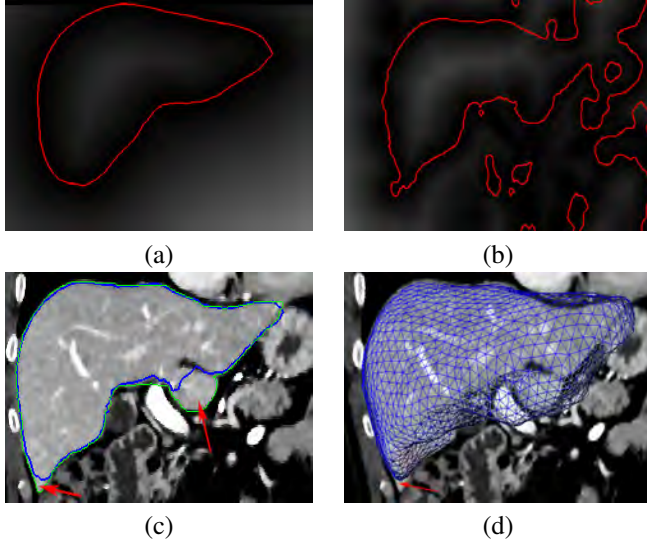
Fig. 5. Shape model initialization. (a) An image representing signed Euclidean distance field of the moved shape model (red curve); (b) An image representing the signed Euclidean distance field of the target boundary (red curve); (c) An obtained initial surface (the blue curve) using the proposed model adaptation algorithm shown in a coronal view, the green curve is the ground truth; (d) The initial surface (blue mesh) in a 3D slice view.

a boundary term which measures Euclidean distance between Ψ_τ and Ψ_λ, Ψ_t; v represents the corresponding vertex on the Ψ_τ, Ψ_λ and Ψ_t; κ controls the balance between region and surface constraints.

A. Model Deformation

For each vertex v_i on a subspace shape model Ψ_λ, boundary candidates are searched along the normal vector n_i of the vertex at discrete positions $j = -n_m, -n_m+1, \cdots, 0, \cdots, n_m-1, n_m$ as

$$v_{ij} = v_i + j\delta n_i \tag{4}$$

where δ is the searching step on the profile. It depends on the size of the liver and the distance between the initial mesh and the boundary. It is computed according to the mean length of edges, which connect the current vertex and its adjacent vertices. n_t is a moving threshold value. n_t describes liver region detection and small structures can be neglected in order to improve the robustness to noise and non-liver structures in the adjacent region. v_i is moved to v_{ij} when vertex v_i is inside the liver (in the foreground of the binary image I_b) and the vertex v_{ij} is searched along the normal vector n_i and $j > n_t$; v_i is moved to v_{ij} when vertex v_i is outside the liver (in the background of the binary image I_b) and vertex v_{ij} is searched along the inverse normal vector $-n_i$ and $|j| > n_t$. n_m is the maximal searching number. The parameter n_m depends on the voxel spacings and the distance between the initial mesh and the boundary. To increase the search range and detect the boundary quickly, n_m can be set to be larger, which may lead to incorrect boundary detection. The cost of mesh deformation can be computed by

$$E_{region} = \frac{1}{N_r} \sum_p (\Gamma_\tau(p) - \Gamma_t(p)) \tag{5}$$

where, N_r denotes a normalization parameter in the local region. In the implementation, signed Euclidean distance field Γ_τ for the deformed mesh and Γ_t for the boundary can be calculated locally for the consideration of time and memory. In some cases, some small holes may exist and deform the signed Euclidean distance field in the target region, normalization by N_r and preprocessing can reduce these influences.

B. Parametric Adaptation

During the process of mesh deformation, the shape model Ψ_λ is also adapted to constrain the deformation of the initial mesh Ψ_τ. The task can be accomplished by minimizing the sum of the surface distances between Ψ_τ and Ψ_λ, Ψ_τ and Ψ_t, which integrate and balance the shape *prior* and image boundary information. The function to minimize is defined as

$$E_{surface} = \frac{1}{N_s} (d(\Psi_\tau(v), \Psi_\lambda(v)) + \omega d(\Psi_\tau(v), \Psi_t(v))) \tag{6}$$

where, N_s denotes a normalization parameter; ω is the weight balancing the shape *prior* and image boundary information.

At the beginning of the deformation, the mesh may be farther from the boundary. The desirable boundaries may accompany some surrounding organs, which may mislead the mesh deformation. To utilize the shape *prior*, parametric adaptation is employed to constrain the mesh deformation. In this condition, the vertex positions are free variables and can be represented as the mean shape and shape variability. The deformed mesh Ψ_τ is registered to the mean mesh $\overline{\Psi}$ using the unit quaternion algorithm [35] and get similarity transformation parameters T and registered mesh $T(\Psi_\tau)$. The displacement $\Delta\Psi$ is computed as

$$\Delta\Psi = T(\Psi_\tau) - \overline{\Psi} = \sum_{m=1}^{M} b_m p_m \tag{7}$$

The weight b_m of the principal mode p_m is computed using the Least Squares method, and then truncate $b_m \in [-\sqrt{3}\lambda_m, \sqrt{3}\lambda_m]$ to get new weight ω_m. A subspace shape model Ψ_λ is generated as

$$\Psi_\lambda = T^{-1}\left(\overline{\Psi} + \sum_{m=1}^{M} \omega_m p_m\right) \tag{8}$$

Eq. (8) allows that the mean shape is deformed and registered to the deformed mesh and make the deformed mesh depend on the shape variability modeling. The whole process is described as Algorithm 1.

VI. DEFORMABLE GRAPH CUT

Deformable graph cut is the key part in our framework whose purpose is to precisely detect the surface of the liver based on the initialized liver shape model. As reported in the literature [18], [21], [22], [26], [28], [37], some sharp structures such as the lateral lobe often exist as shown in Fig.5, which makes it difficult to extract using these methods. The deformable graph cut can be considered as an optimization process aimed at progressively finding the optimal surface with a minimal cost. It effectively integrates the shape information

Algorithm 1 Model Adaptation.

Require:

A coarse contour of organs represented by a binary image I_b; The mean mesh, $\overline{\Psi}$; The principal modes, $p_m, m = 1, 2, \cdots, M$; The weights of the principal modes, $\lambda_m, m = 1, 2, \cdots, M$; The balance parameter, κ; The moving threshold value, n_t; The maximal searching number, n_j; The balancing weight, ω; Energy threshold value, E_t.

Ensure:

Adapted liver mesh, Ψ_τ.

1: Compute $\Gamma_t(p)$ by performing EDT for interior and exterior of I_b, and find the coordinates $\vec{p}_c$ of the voxel with the minimal signed Euclidean distance;

2: Compute the center of the mean mesh $\overline{\Psi}$, move it to $\vec{p}_c$ and then get the initial mesh Ψ_τ;

3: Initialize energy, $E_b \leftarrow \infty$;

4: **for** v_i on the mesh on Ψ_τ **do**

5: Compute the mean length l of adjacent edges of vertex v_i, and then obtain the searching step $\delta = l$;

6: Sample vertices along the normal vector n_i of Ψ_τ according to Eq. (4);

7: **if** v_i is in the background of I_b **then**

8:   Search the first vertex v_{ij} in the foreground of I_b along n_i from v_i, and get the number j;

9: **else**

10:   Search the first vertex v_{ij} in the background of I_b along $-n_i$ from v_i, and get the number j;

11: **end if**

12: $v_i \leftarrow v_{ij}$, if $|j| > n_t$;

13: **end for**

14: Convert the deformed mesh Ψ_τ to a binary image and compute the signed Euclidean distance field $\Gamma_\tau(p)$;

15: Compute the mesh deformation cost $E_{region}(p)$ according to Eq. (5), N_r is the maximal distance; Compute the surface distance $d(\Psi_\tau(v), \Psi_t(v))$;

16: Register the deformed mesh Ψ_τ to the mean mesh $\overline{\Psi}$ and get similarity transformation parameters T and registered mesh $T(\Psi_\tau)$;

17: Compute displacement $\Delta\Psi \leftarrow T(\Psi_\tau) - \bar{\Psi}$;

18: Compute the weight b_m of the principal mode p_m using the Least Squares method, and truncate $b_m \in [-\sqrt{3}\lambda_m, \sqrt{3}\lambda_m]$ to obtain the new weight ω_m;

19: Compute the subspace shape model Ψ_λ according to Eq.(8) with the weight ω_m;

20: Compute $E_{surface}(v)$ according to Eq.(6);

21: Compute $E(p, v)$ according to Eq.(3);

22: $\Delta E \leftarrow E_b - E(p, v)$, $E_b \leftarrow E(p, v)$;

23: If $|\Delta E| < E_t$, $\Psi_\tau \leftarrow \Psi_\lambda$, and then go to step 4; else, get Ψ_τ and stop.

with the globally optimal 3-D delineation capability of the graph cut method [6]. The three major components are graph construction, cost function design and optimal surface detection. Graph construction and cost function design are usually carried out in one step to effectively integrate the properties and inter-relationship of the input images and shape *prior*. After the graph is constructed, the desirable surface can be detected by applying the traditional graph cut algorithm [6].

A. Graph Construction

After the mean shape is deformed using the proposed model adaptation method, an initial surface Ψ_τ can be obtained and then a weighted directed and irregular graph $\mathcal{G}$ is constructed in a narrow band around Ψ_τ. With the improvement of CT scanners, higher resolution can be reached in CT images, which leads to sharp increase in memory usage [21], [38]. Unlike the traditional graph construction algorithms which built a regular graph for the entire image [21], [22], [26], [28], [37], our graph construction strategy enables the construction of a deformable graph according to the initial surface properties.

The graph construction process is illustrated in Fig. 6. For each vertex v_i on the mesh Ψ_τ, a column of equidistant points is sampled along the gradient of the signed Euclidean distance field. In order to detect the desirable surface especially in the shape region, points sampled along the normal direction may lead to incorrect local surface propagation. To address this issue, a novel graph is constructed and consists of three types of nodes $\mathcal{V} = \{\mathcal{T}, \mathcal{N}, \mathcal{S}\}$ and four types of weighted arcs $\mathcal{E} = \{E_a, E_r, E_t, E_s\}$. A sink node $\mathcal{T}$ represents a set of voxels in the interior of Ψ_τ, whose distance value is smaller than a threshold value d_{min}; a source node $\mathcal{S}$ represents a set of voxels in the exterior of Ψ_τ, whose distance value is larger than a threshold value d_{max}. The distance value is negative in the interior of Ψ_τ and vice versa. The node set $\mathcal{N}$ corresponds to sampled points in the signed Euclidean distance field of the mesh Ψ_τ. At the beginning of the sampling, the points correspond to vertices in mesh Ψ_τ. The subsequent points are sampled along the local gradient of the signed Euclidean distance field started from mesh Ψ_τ, as shown in Fig.6(a). The columns in graph $\mathcal{G}$ are formed as

$$\begin{cases} v_{i,j+1} = v_{i,j} + \Delta \cdot g_{i,j}, \\ j = -n_g, -n_g + 1, \cdots, 0, \cdots, n_g - 1, n_g, \\ n_g = \frac{N_g - 1}{2}. \end{cases} \quad (9)$$

where, $v_{i,j}$ is the jth node in the ith column of the graph, $v_{i,0}$ is the vertex of the initial surface; Δ is the sampling step; and $g_{i,j}$ is the gradient of node $v_{i,j}$ in the signed Euclidean distance field. N_g is the number of sampling points.

As shown in Fig.6, the arc set $\mathcal{E}$ contains four types of weighted arcs: intra-column arcs E_a, inter-column arcs E_r, sink arcs E_t and source arcs E_s. An intra-column arc in E_a connects unidirectionally and inwardly two successive nodes in a column generated from a vertex on the initial mesh. An inter-column arc in E_r connects two nodes on two adjacent columns. A sink arc in E_t unidirectionally connects each node in $\mathcal{N}$ to the sink node $\mathcal{T}$. A source arc in E_s unidirectionally connects source node $\mathcal{S}$ to each node in $\mathcal{N}$. The arcs in graph $\mathcal{G}$ are defined as

$$\mathcal{E} = \begin{cases} E_a = \{e(v_{i,j}, v_{i,j+1})\} \\ E_r = \{e(v_{i,j}, v_{l,j+k})\} \\ E_s = \{e(\mathcal{S}, v_{i,j})\} \\ E_t = \{e(v_{i,j}, \mathcal{T})\} \end{cases} \quad (10)$$

(a)

(a) (b)

Fig. 7. Final liver segmentation. (a) The red curve represents the final segmentation of the liver; the green curve represents ground truth; (b) The corresponding final liver segmentation in a 3D slice view.
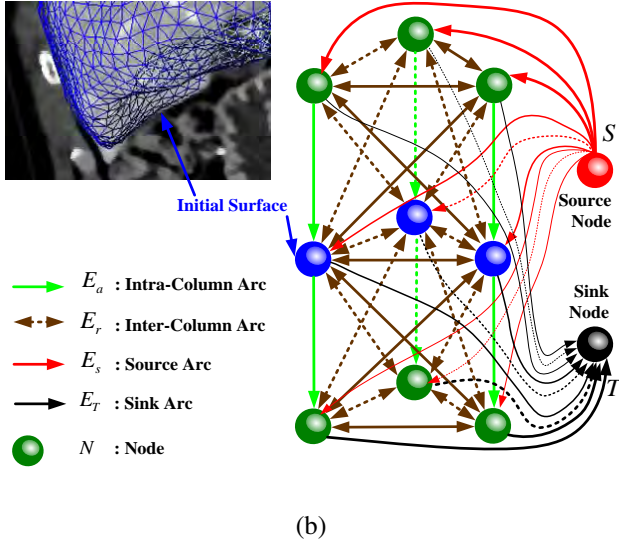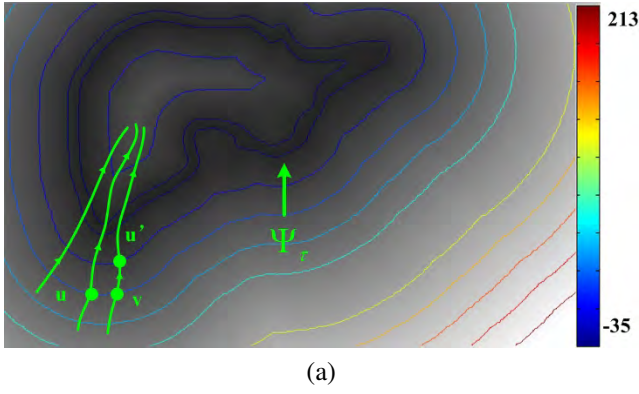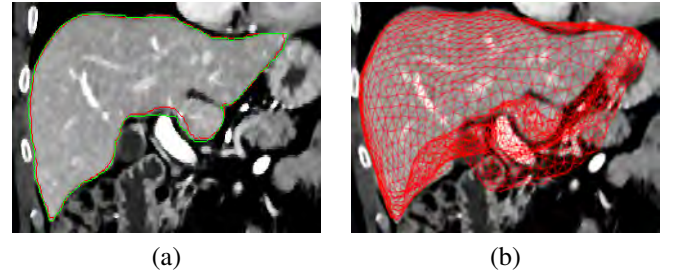

(b)

Fig. 6. Illustration of the deformable graph cut. (a) The gray image representing the signed Euclidean distance field of the initialized mesh, where the three green curves denote deformable sampling paths for graph construction and the rest of the curves are iso-contours of the signed Euclidean distance field; (b) A deformable graph from the initialized mesh.

where, $v_{l,j+k}$ shows the node adjacent columns, $j = -n_g, -n_g + 1, \cdots, 0, \cdots, n_g - 1, k = 0, \pm 1, \cdots, \pm \Delta_k$, Δ_k is the spatial smoothness constraints.

B. Cost Function Design

The deformable graph cut is driven by cost functions associated with the graph vertices, which reflect properties of the initial surface. Derived from the traditional graph cut [5]–[7], the deformable graph cut can be defined as an energy minimization problem. For a set of nodes $\mathcal{N}$ and a set of labels $\mathcal{L}$, the goal is to find a labeling $f : \mathcal{N} \to \mathcal{L}$ such that the surface of an object can be detected by minimizing the energy function $E(f)$.

In our framework, for each node $v_{i,j}$ (denoted by v) in the node set $\mathcal{N}$, the region cost is the sum of a data penalty term $D(f_v)$, which is constrained by a shape region penalty term $S_r(d_v)$. The data term is defined according to image intensity and can be considered as a cluster likelihood of image intensity for the target object. The boundary term $B(f_v, f_u)$ is also based on image intensity, which is also constrained by a shape boundary penalty term $S_b(d_v, d_u)$. The shape region

term and the shape boundary penalty term are both dependent on the signed Euclidean distance field corresponding to the initial shape. The proposed shape-constrained energy function is defined as,

$$E(f) = \sum_{v \in \mathcal{N}} (D(f_v) \cdot S_r(d_v)) + \sum_{v \in \mathcal{N}, u \in n_v} \chi \cdot B(f_v, f_u) \cdot S_b(d_v, d_u) , \quad (11)$$

where, $u \in n_v$ denotes adjacent nodes of v corresponding to E_a and E_r. The parameter χ controls the balance between the region cost and boundary cost. These terms, which correspond to the weights of the four types of arcs $\mathcal{E} = \{E_a, E_r, E_t, E_s\}$, are defined as follows:

$$D(f_v) = \begin{cases} \exp\left(-\frac{(I_s - I_v)^2}{2\sigma_s^2}\right), & e(\mathcal{S}, v) \in E_s; \\ \exp\left(-\frac{(I_v - I_t)^2}{2\sigma_t^2}\right), & e(v, \mathcal{T}) \in E_t. \end{cases} , \quad (12)$$

Voxels in the original image were considered as foreground seeds and background seeds, whose distances are respectively smaller and larger than given values in the signed Euclidean distance field, e.g., 50% of the minimal distance and maximal distance. The seeds were then clustered using K-means. I_s and I_t were intensities of the clustered center in the N_c clusters. I_v is the intensity of a node. The differences $(I_s - I_v)^2$ and $(I_v - I_t)^2$ are respectively computed and the minimal values are used for the computation of $D(f_v)$ in Eq.(12). σ_s, σ_t are the standard deviation of the intensity differences between sampled points and foreground seeds, background seeds respectively.

$$S_r(d_v) = \begin{cases} \exp\left(\frac{d_v}{d_{\max}}\right), & d_v \le d_{\max}, j < n_g, \\ & e(S, v) \in E_s; \\ \infty, & d_v > d_{\max}, or, j = n_g, \\ & e(S, v) \in E_s; \\ \exp\left(\frac{d_v}{d_{\min}}\right), & d_v \ge d_{\min}, j > -n_g, \\ & e(v, T) \in E_t; \\ \infty, & d_v < d_{\min}, or, j = -n_g, \\ & e(v, T) \in E_t. \end{cases} , \quad (13)$$

where, d_v represents distance of the sampled nodes in the signed Euclidean distance field Γ for the current surface. $d_{\min}, d_{\max}$ are parameters of the minimal distance and maxi-

Algorithm 2 Deformable Graph Cut.

Require:

    The enhanced image, I_E; Adapted liver mesh, Ψ_τ; Distance percent $(0-1)$, p_d; Number of K-means clusters, N_c; The sampling points number, N_g; Mesh subdivision parameter, t_s; The standard deviations, $\sigma_s, \sigma_t, \sigma_u, \sigma_d$; The spatial smoothness constraints, Δ_k; The balance parameter, χ; Surface distance threshold value, E_d.

Ensure:

    Detected liver surface, Ψ_o.

1: Subdivide adapted liver mesh Ψ_τ using the butterfly subdivision algorithm [39], compute its bounding box and broaden it with $N_p = 20$ voxels in the six end points;

2: Convert Ψ_τ to a binary image in the broaden bounding box and compute the signed Euclidean distance field $\Gamma_\tau(p)$;

3: Create foreground seeds $(d < d_{min} \leftarrow p_d \cdot D_{min})$ and background seeds $(d > d_{max} \leftarrow p_d \cdot D_{max})$, D_{min} and D_{max} are the minimal and maximal distance in $\Gamma_\tau(p)$;

4: Apply K-means to the gray values of the seeds, and obtain K mean intensities for foreground seeds and background seeds respectively;

5: **for** v_i on the mesh on Ψ_τ **do**

6:     Compute the mean length l of edges for vertex v_i, and then obtain the searching step $\Delta \leftarrow l$;

7:     Compute the normalized gradient $g_{i,j}$ of node $v_{i,j}$ in $\Gamma_\tau(p)$;

8:     Sample vertices along $g_{i,j}$ according to Eq. (9);

9: **end for**

10: Create graph $\mathcal{G}$ according to Eq. (10);

11: **for** v in the node set $\mathcal{N}$ **do**

12:     Compute the weight ϖ of E_s according to Eq. (12) and Eq. (13): If $d > d_{max}$ or $j = n_g$, then $\varpi \leftarrow \infty$; Else compute $(I_s - I_v)^2$ and select the smallest value;

13:     Compute the weight ϖ of E_t according to Eq. (12) and Eq. (13): If $d < d_{min}$ or $j = -n_g$, then $\varpi \leftarrow \infty$; Else compute $(I_v - I_t)^2$ and select the smallest value;

14:     Compute the weight ϖ of E_a, E_r according to Eq. (14) and Eq. (15);

15: **end for**

16: Optimize energy function Eq. (11) by using the traditional graph cut algorithm;

17: **for** $j \leftarrow -n_g, \cdots, n_g$ for each column of v_i **do**

18:     if $L(v) = source$, and then $v_i \leftarrow v$;

19: **end for**

20: Simplify the adapted mesh Ψ_τ' by using the quadric error metric algorithm [35], and smooth the adapted mesh Ψ_τ' by using Laplacian Smoothing algorithm [40];

21: Compute the mean surface distance $d_e \leftarrow d(\Psi_\tau', \Psi_\tau)/V_m$; If $d_e > E_d$, $\Psi_\tau \leftarrow \Psi_\tau'$ and go to step 1; else $\Psi_o \leftarrow \Psi_\tau'$ and stop.

---

mal distance, $d_{\min} \leq 0, d_{\max} \geq 0$.

$$B(d_v, d_u) = \exp\left(-\frac{(I_v - I_u)^2}{2\sigma_u^2}\right), e(v,u) \in \{E_a, E_r\},$$

(14)

where, I_u represents intensity of the adjacent sampled nodes

of v, σ_u is the standard deviation of the intensity differences between sampled nodes v and u.

$$S_b(d_v, d_u) = \exp\left(-\frac{(d_v - d_u)^2}{2\sigma_d^2}\right), e(v,u) \in \{E_a, E_r\}.$$

(15)

where, d_v, d_u are the distances in Γ of sampled nodes v and u, and σ_d is the standard deviation of the distance differences between sampled nodes v and u. As illustrated in Fig.6(a), if an adjacent sampled node u and the current node v are on the same iso-surface in Γ, then the two nodes should both be on the same target surface or be given the same segmented label; otherwise, if an adjacent sampled node u' and the current node v are on different iso-surfaces in Γ, the same target surface may be detected between them.

In this phase, the initial surface ia the adapted liver mesh Ψ_τ by using the model adaptation algorithm. The weighted $\mathcal{G}$ is constructed by using Algorithm 2, detection of the target surface is then formulated as finding a minimum cut. This can be solved by the max-flow/min-cut algorithm [6]. The process can be iteratively employed to search the desirable surface of the liver based on the previous adapted liver mesh Ψ_τ'. The algorithm is stopped when the distance between the adapted liver meshes Ψ_τ and Ψ_τ' is lower than a threshold value E_d. Results of the extracted liver surface are shown in Fig. 7, as optimized from the initialized shape in Fig. 5.

TABLE I
PARAMETER SETTINGS

Steps	Parameter Settings
Preprocessing	Landmarks $\mathcal{V} = 2502$, $M = n_f = 30$ for SLIVER07, $M = n_f = 20$ for 3Dircadb, $\lambda_a = 10$, $t_a = 0.03$, $n_a = 4$;
Model Initialization	$r_o = 2$, $r_c = 10$, $\kappa = 125$ $n_j = 20$, $n_t = 5$, $\omega = 1$, $E_t = 0.001$;
Deformable Graph Cut	$p_d = 0.5$, $N_c = 10$, $t_s = 40$, $N_g = 20$, $\Delta_k = 2$, $\chi = 10$, $\sigma_d = 0.5$, $\sigma_s = \sigma_t = \sigma_u = 1$, $E_d = 0.01$.

VII. EXPERIMENTAL RESULTS

A. Evaluation Methods

1) Subject Data: To evaluate the accuracy and performance of the proposed method, it was tested on two clinical contrast-enhanced CT data sets, which are publicly available. The first data set was SLIVER07 [1], which contains 30 contrast-enhanced CT images (20 training scans and 10 test scans). The pixel size varied from 0.54 to 0.86 mm, slice thickness from 0.7 to 5 mm, in-plane resolution of 512×512 pixels, and slice number 64 to 502. The second data set was 3Dircadb [2], which contains 20 contrast-enhanced CT images. The pixel size varied from 0.56 to 0.86 mm, slice thickness from 1 to 4 mm, and slice number 184 to 260. The ground truth was provided by experienced experts. The two sets were alternatively chosen as the training set and test data.

---

[1] http://sliver07.org/download.php
[2] http://beta.ircad.fr/softwares/3Dircadb/3Dircadb1/index.php?–lng=en

2) Evaluation metrics: To quantitatively evaluate the performance of our proposed method, we compared the segmentation results with the ground truth according to the following five volume and surface based metrics [41]: volumetric overlap error (VOE), signed relative volume difference (SRVD), average symmetric surface distance (ASD), root mean square symmetric surface distance (RMSD), and maximum symmetric surface distance (MSD). The volume and surface based metrics are given in percent and millimeters, respectively. For all these evaluation metrics, the smaller the value is, the better the segmentation result.

3) Parameter Settings: In this section we will review detailed parameter settings for each step, where Table I lists all of the parameter settings. The number of landmarks and vertices of the initial shape model was $\mathcal{V} = 2502$. The mean shape model of SLIVER07 was obtained from manual segmentation by experienced experts and applied to 3Dircadb for shape adaptation; The mean shape model of 3Dircadb was obtained from manual segmentation by experienced experts and applied to SLIVER07 for shape adaptation. During smoothing by curvature anisotropic diffusion filtering, the conductance parameter λ_a was set at 10, the time step t_a was around 0.03, and the number of iterations n_a was typically set to 4. Apply morphological opening with round structuring elements ($r_o = 2$) to remove small structures, and then apply morphological closing with round structuring elements ($r_c = 10$) to connect the disjointed regions or fill holes. $\kappa = 125$ typically can control the balance between region and surface constraints. In our experiments, the voxel spacing range was 0.54mm to 5.0 mm, $n_m = 20$ and $n_t = 5$ were appropriate to efficiently deform the initial surface. For the consideration of memory, the number of sampling points N_g was set 40, since the initialized mesh was remeshed and subdivided into dense meshes with about $V_m = 40002$ vertices ($t_s = 40$) for the accurate detection of the target surface using the proposed deformable graph cut. The standard deviations of the intensity $\sigma_s, \sigma_t, \sigma_u$ were set at 1. The interval for the standard deviation of the distance differences σ_d can be $[0.1, 2]$, or typically 0.5. The balance parameter χ was set at 10. The parameters described in this section were determined experimentally, but the detection was not very sensitive to their exact values. The values described here were mainly motivated by performance considerations. Our method was implemented in C++ and tested on a 32-bit desktop PC (3.1 GHz Core(TM) i5-3450 CPU and 4 GB RAM).

B. Validation Results

1) Case Study: During the experiments, the EDT based method can be successfully applied to quickly localize the coarse position of the liver. Fig.8 shows the whole process using the proposed method in a CT image of the abdomen and chest in database Sliver07. The initialized surface and final surface are shown in Fig.8 (c) and (d) respectively.

Fig.9 (a)-(e) shows the mean shape model was iteratively adapted to boundary of the liver. The green curves were manual segmentation. The yellow curve in Fig.9 (a) is the mean shape using the EDT based method. The surface was far from the boundary of the liver and part of the model was in the exterior of the liver. In the first iterations of model adaptation, the shape model was adjusted to the boundary of the right hepatic lobe and then driven to the boundary of the left hepatic lobe. However, it is difficult to detect boundaries of sharp structures in both the right hepatic lobe and left hepatic lobe. On the one hand, model adaptation was constrained by a PDM from statistical shapes, which can not contain enough shape variability of the livers; on the other hand, the model was adapted along its normal direction which was difficult to reach along those boundaries of the sharp structures.

Fig.9 (f)-(h) shows iterations using the deformable graph cut. To detect target boundaries of livers more accurately, the proposed deformable graph cut can detect target boundaries with consideration of a region cost and boundary cost. As can be seen in Fig.9 (f), the smooth surface was detected. With the integration of shape *prior*, the surface was progressively adapted to the target boundaries even if structures were sharp. This is because the mesh was remeshed and adjusted along a deformable distance field.

2) Effect of Different Parameters: Fig.10 shows the impact of shape σ_d of the deformable graph cut. Fig.9 (f)-(h) shows segmentation using different values $\sigma_d = 1, 0.5, 0.3$. As the value becomes larger, segmentation tends to include non-hepatic tissues with similar intensity, which often occurs using the traditional graph cut. As can be seen in this test, the proposed deformable graph cut can control the balance between the region and boundary by the integration of shape *prior* more robustly, as illustrated in Fig.6(a).

3) Challenging Cases: Fig.11 shows three challenging cases. The first row shows the segmentation of a CT image from database 3Dircadb. There are 20 tumors in this CT image. Besides, numerous sharp regions and divided lobes exist, as can be seen in Fig.11(a). As shown in Fig.11(a)-(b), model adaptation can be applied to reach most of the target boundary. Some sharp structures were lost in the left lobe and near the vessel. The maximal distance to target boundary was 21.82mm. With the help of deformable graph cut, those sharp structures can be included, as shown in Fig.11(c)-(d). The maximal distance to the target boundary decreased to 18.87mm. The second row shows the segmentation of a CT image from database Sliver07. As shown in Fig.11(c), the subject was laid on one side, which led to a large rotation with regard to the mean shape model. Besides, a large gap also exist. These two difficulties made it difficult to reach the boundary of the left lobes for the shape model based adaptation method, which led to 52.38mm of the maximal distance to the target boundary. After the initial surface was adapted using the deformable graph cut, the maximal distance was decreased to 19.25mm, as shown in Fig.11(h). The third row shows the segmentation of a CT image from database 3Dircadb. There are 2 large tumors in this CT image. As can be seen in Fig.11(i), model adaptation stopped moving towards the boundary of the liver. Large surface difference was generated between the initialized liver and manual segmented liver near the regions of the tumors as shown in Fig.11(j). The distance was then decreased to 34.59mm using the proposed deformable graph cut as shown in Fig.11(l).
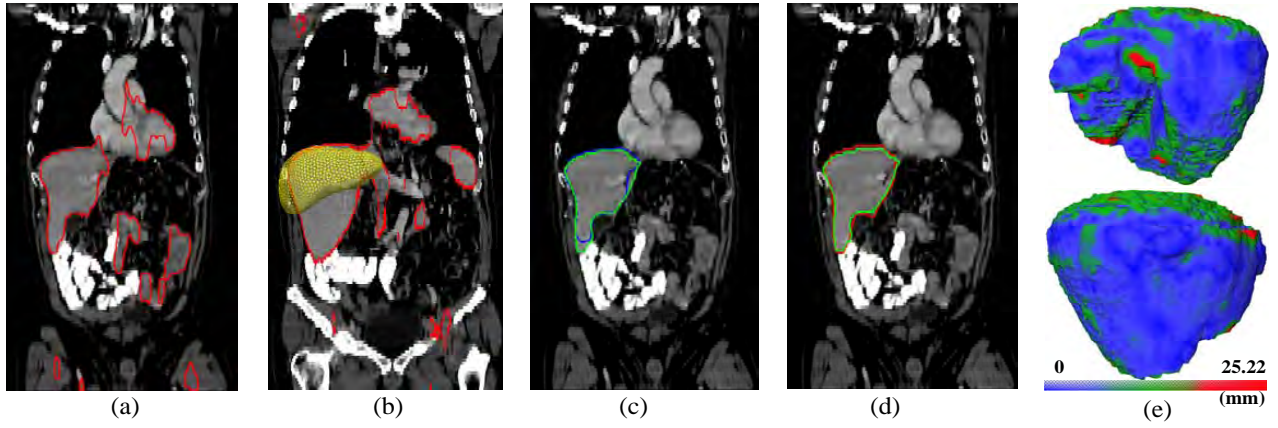
Fig. 8. Liver initialization and segmentation in a CT image of abdomen and chest. (a) The red curve represents preprocessed boundaries; (b) Moved shape model (yellow surface) using an EDT based method; (c) Initialized liver based on model adaptation (blue curve); (d) The red curve represents final segmentation of liver, the green curve represents ground truth; (e) The surface distance of corresponding liver final segmentation to manual segmented liver surface.
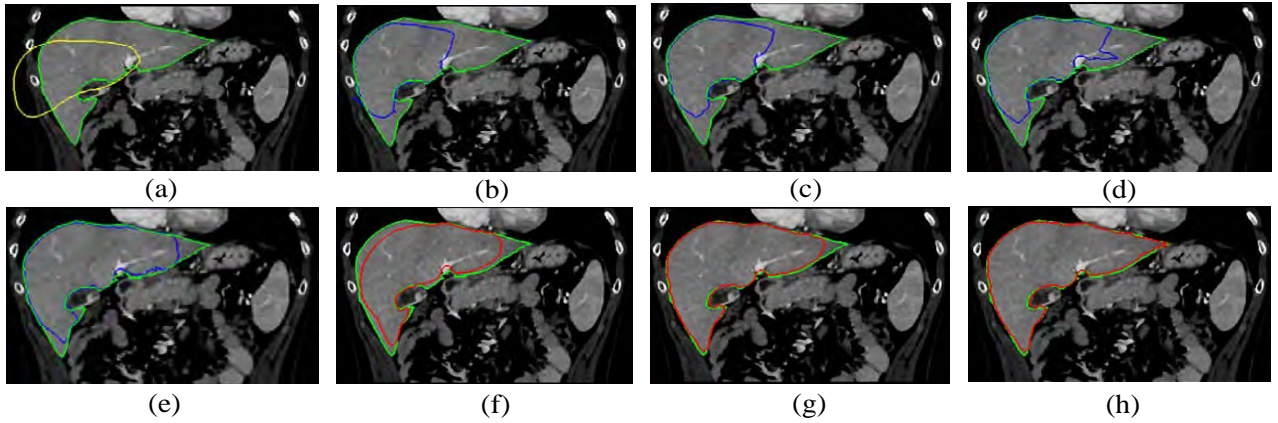

Fig. 9. Iterative initialization based on model adaptation and segmentation using the deformable graph cut in a CT image in Sliver07 Database. Manual segmentation is shown in green curves. (a) Moved mean shape model (yellow curve); (b)-(e) The 1st, 3rd, 7th and 11th iterations of model adaptation (blue curves); (f)-(h) The 1st, 2nd and 5th iterations of the deformable graph cut (red curves).
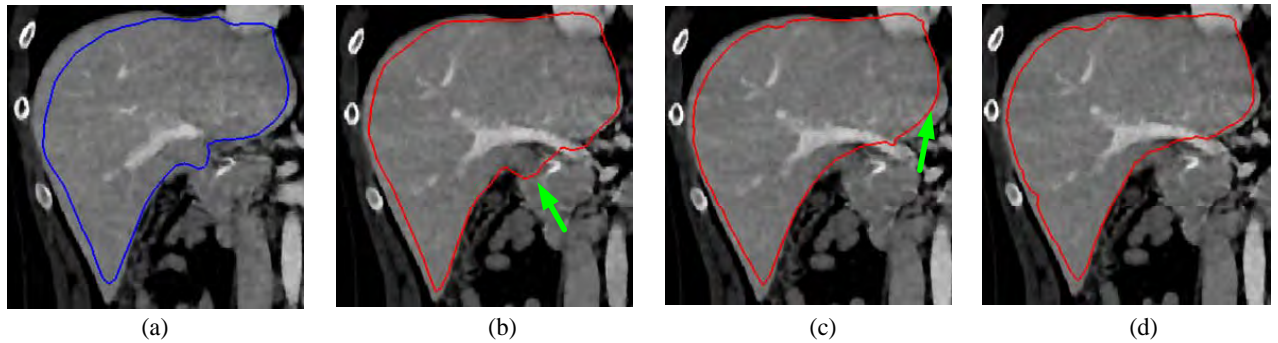

Fig. 10. The parameter σ_d of deformable graph cut. (a) Initialized liver based on model adaptation (blue curve); (b)-(d) $\sigma_d = 1, 0.5, 0.3$ using deformable graph cut (red curves).

4) Quantitative Results and Comparisons: To assess the performance of the proposed liver segmentation framework within the larger context of the existing literature, two tests were done to compare it with recently published methods based on the Sliver07 database and 3Dircadb database. Results for each measure represent as the mean and standard deviations of the overall datasets.

Table II shows the quantitative comparative results of the liver segmentation with previous methods in [17], [18], [26], [42], [43] and the proposed liver shape initialization and segmentation based on the Sliver07 database. As can be seen in the 6th row of Table II, model initialization was far from the accurate segmentation of the liver. Large distance to manual segmentation can be seen in the measures of ASD, RMSD
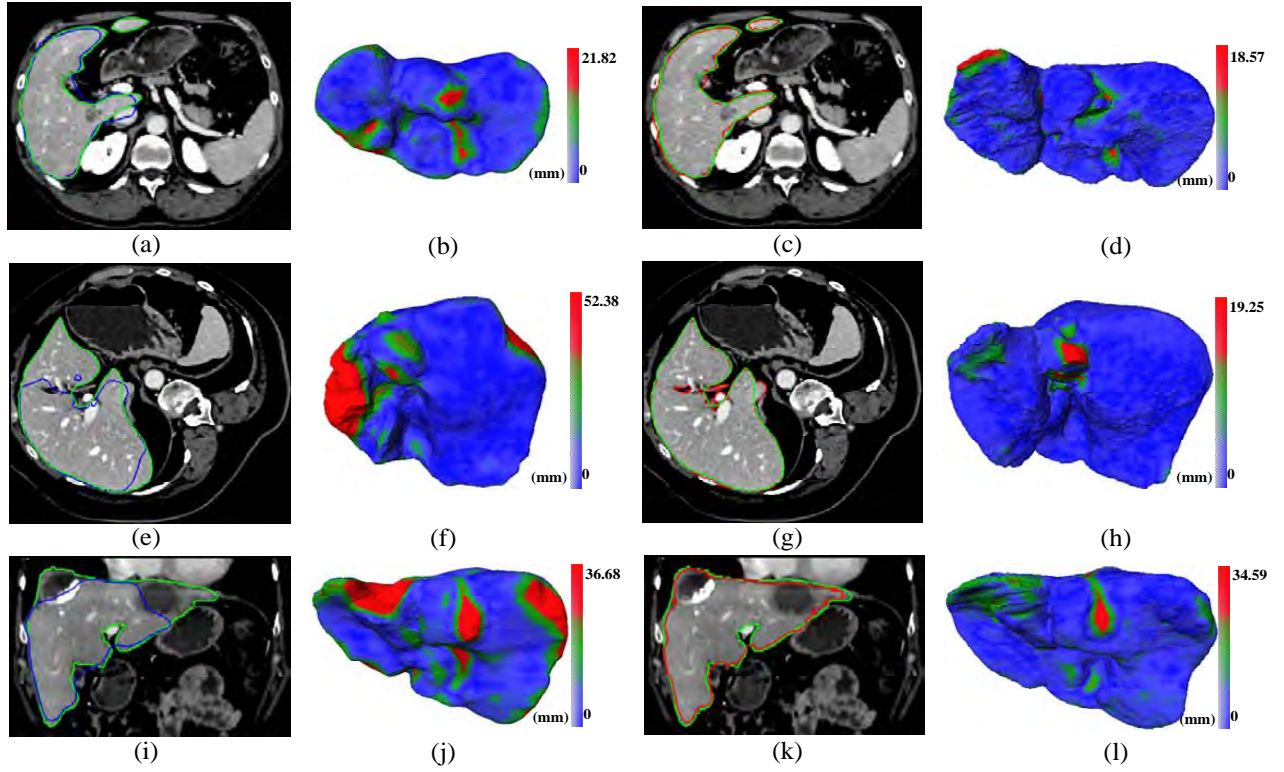
Fig. 11. Some challenging cases. Manual segmentation is shown in green curves; initialization is shown in blue curves, final segmentation is shown in red curves. The first column shows initialization based on model adaptation; the second column shows distance between the initialized surfaces to manual segmented surfaces; The second shows segmentation using deformable graph cut; the fourth column shows distance between the final detected surfaces to manual segmented surfaces. The images in the 1st and 2nd rows are from Sliver07 Database, the image in the 3rd are from 3Dircadb Database.

TABLE II
QUANTITATIVE COMPARATIVE RESULTS FOR THE SLIVER07 DATABASE. RESULTS ARE REPRESENTED AS MEAN AND STANDARD DEVIATION. NA
STANDS FOR INFORMATION NOT AVAILABLE.

Sliver07	VOE[%]	SRVD[%]	ASD[mm]	RMSD[mm]	MSD[mm]	Time
Wimmer[42]	8.1±1.1	6.1±2.6	1.30±0.2	2.2±0.4	18.7±4.6	4-7min
Linguraru[41]	6.47±0.97	1.04±2.83	1.02±0.16	2.00±0.36	18.32±4.91	15min
Kainmüller[17]	6.96±2.34	-3.57±3.38	1.10±0.34	2.25±0.68	20.95±6.41	3min
Chen[25]	6.5±1.8	-2.1±2.3	1.0±0.4	1.8±1.0	20.5±9.3	6min
Zhang[18]	5.25	0.73	0.93	2.23	24.80	2.86min
Initialization	14.83±7.88	-9.29±8.58	3.08±2.11	5.62±3.75	31.74±14.71	193±102.67s
Final Segmentation	6.24±1.52	1.18±2.76	1.03±0.31	2.11±0.95	18.82±8.82	91.95±21.26s

and MSD. The SVRVD was $-9.29\% \pm 8.58\%$, which means that it tends to under-segment the liver tissue, as shown in Fig.8-Fig.11. For all the datasets, our method achieved much better performance than Kainmüller's method even though they employed an SSM based approach.

As can be seen in the 4th row, Chen's method tended to obtain a under-segmented liver based on their shape constrained graph cut (the 2nd column of Fig.12), which integrated shape prior into region term only. The maximal surface distance of Zhang's method is $24.8mm$. Surface detection proposed by Zhang $et.$ $al.$ was applied along the normal direction

of surfaces, which also made it difficult to avoid under-segmentation and over-segmentation, as shown in the 3rd column of Fig.12.

Table III shows the quantitative comparative results of the liver segmentation with previous methods in [44]–[46] and the proposed liver shape initialization and segmentation based on the 3Dircadb database. For shape initialization results, model initialization was also far from accurate segmentation of the liver. Similarly, large distance to manual segmentation could be seen in the measures of ASD , RMSD and MSD, as can be seen in the 4th row of Table III. For all of the datasets,
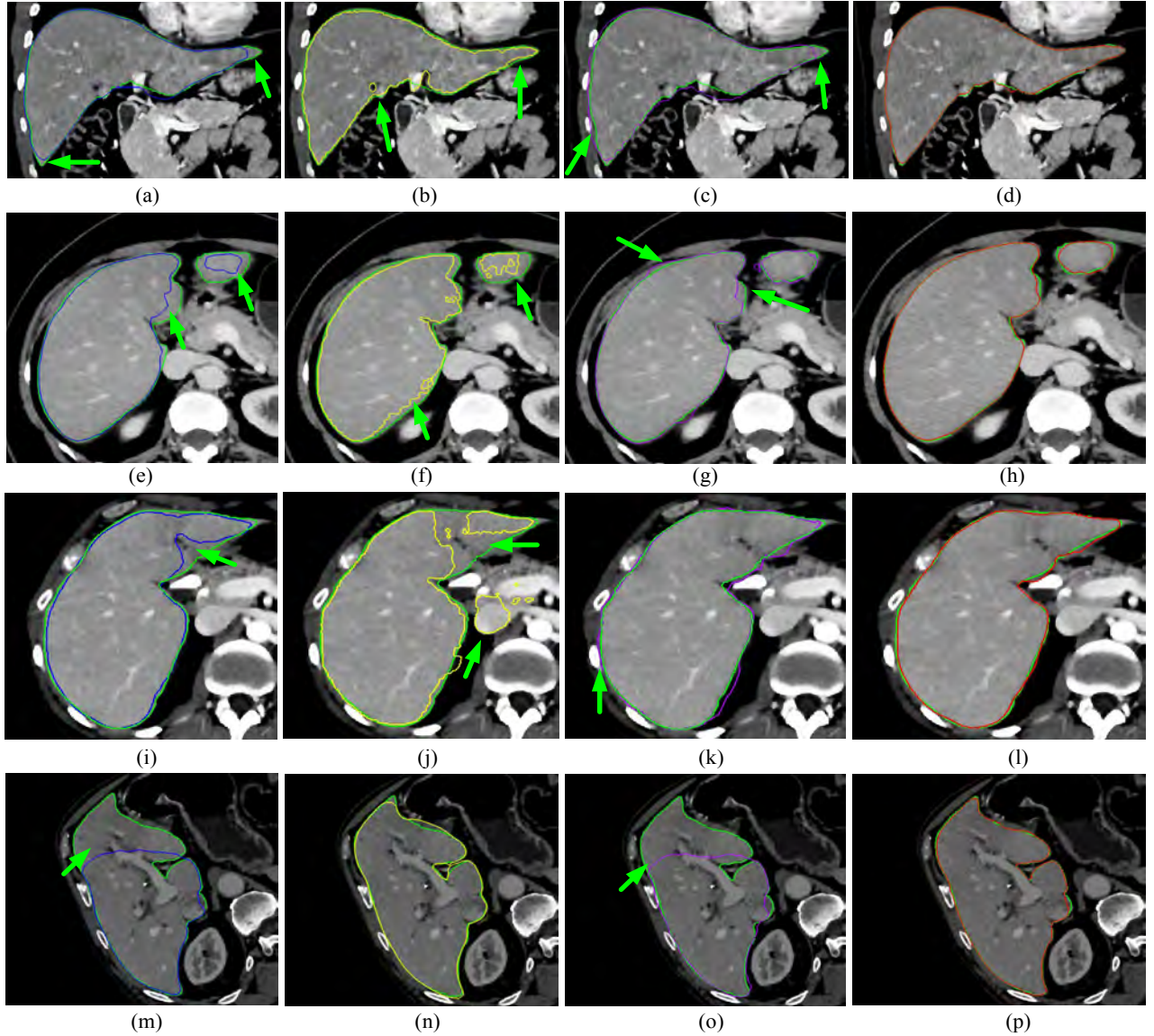
Fig. 12. Segmentation Comparisons in Sliver07 Database. Manual segmentation is shown in green curves. The first column shows initialization based on the model adaptation method; The 2nd column shows segmentation by using Chen's shape constrained graph cut; The 3rd column shows segmentation by using Zhang's graph search; The 4th column shows segmentation by using proposed deformable graph cut.

the proposed method achieved much better performance than Chung's method except for MSD. With regards to SRVD, Chung's method and Kirschner's method tended to under-segment livers since there were numerous tumors in those CT images. A large MSD of Kirschner's method achieved $34.6mm \pm 17.7mm$. For most measures, the proposed method showed slightly better performance than Kirschner's method and Erdt's method.

Table II and Table III also showed the running time of the testing stage (i.e., shape initialization and final segmentation). With regards to the Sliver07 database, the average computation time of the proposed method was about 5min. With regards to the 3Dircadb database, the proposed method took about 3min.

VIII. DISCUSSION AND CONCLUSIONS

In this paper, a novel approach has been proposed for automatic liver segmentation, which effectively integrates the

shape based initialization and the deformable graph cut method with incorporation of shape constraints. This approach is able to tackle the problems brought on by the special characteristics of the liver's anatomical structure and image quality. To demonstrate higher performance, the proposed method was evaluated on 50 CT scan images, which are publicly available. The experimental results showed that the proposed method was effective and accurate for progressive detection of the liver surface. Compared to previous methods, the proposed method can detect the hepatic surfaces more accurately, and can successfully cope with under-segmentation and over-segmentation.

In order to make the proposed method automatic, a heuristic and fast EDT based method was applied to estimate the coarse position of the liver in a test image. As can be seen from the experiments on the two public databases Sliver07 and

TABLE III
QUANTITATIVE COMPARATIVE RESULTS FOR THE 3DIRCADB1 DATABASE. RESULTS ARE REPRESENTED AS MEAN AND STANDARD DEVIATION. NA
STANDS FOR INFORMATION NOT AVAILABLE.

3Dircadb	VOE[%]	SRVD[%]	ASD[mm]	RMSD[mm]	MSD[mm]	Time
Chuang[43]	12.99±5.04	-5.66±5.59	2.24±1.08	NA	25.74±8.85	NA
Kirschner[44]	NA	-3.62±5.50	1.94±1.10	4.47±3.30	34.60±17.70	41±3.8s
Erdt[45]	10.34±3.11	1.55±6.49	1.74±0.59	3.51±1.16	26.83±8.87	45s
Initialization	15.13±4.56	-8.37±6.64	3.43±2.14	6.98±5.37	42.31±24.27	81.45±45.91s
Final Segmentation	9.15±1.44	-0.07±3.64	1.55±0.39	3.15±0.98	28.22±8.31	97.11±12.76s

3Dircadb, this approach was able to move the mean shape model correctly. In order to drive the mean shape model close to the boundaries of the livers, the initial mesh was locally and iteratively deformed to the target boundary, which was constrained to stay close to a subspace of shapes describing the anatomical variability. In order to detect the liver surface more accurately, the proposed deformable graph cut could effectively integrate the properties and inter-relationship of the input images and initialized surface, which allowed the progressive finding of the target surface of the liver in a narrow band with a minimal cost algorithm.

There are three differences between the proposed deformable graph cut and Chen's method [26]. 1) Compared to Chen's method, shape constraints were integrated into boundary term, which also improves the power of boundary constraints. As can be seen in Fig.12, incorrect boundaries of the livers were found by using Chen's method, which may produce under-segmentation or over-segmentation. 2) Traditionally, $n-links$ bidirectionally connected adjacent nodes, which is suitable for region segmentation. The inter-column and intra-column arcs were introduced such that the surfaces of the livers were definitely detected in each column. This improves the power of boundary constraints. 3) Each node corresponded a voxel in the test image in Chen's graph, which will consume huge amount of memory as resolutions of CT images increase, as pointed in [21], [38]. The proposed method sampled a few voxels by linear interpolation in a narrow band of the initial surface, which may need less amount of memory, as discussed in our previous paper [38].

There are also three differences between the proposed deformable graph cut and graph search method [18], [19]. 1) The intra-column arcs were bidirectional. This encourages the connection of adjacent columns and avoids under-segmentation as shown in Fig.12(c) and (g). 2) Compared to graph search, each node in the graph connected both S and T in the proposed method. Nodes with positive weights only connected S, while those with negative weights only connected T in graph search. This strategy may reduce the region constraints. This may lead to under-segmentation by using graph search, as shown in Fig.12 (c), (g) and (o). In addition, weights of the arcs were set to infinity when the nodes on the top and bottom of the graph were connected S and T respectively, or the distance was larger/smaller than $d_{max}d_{min}$. This can avoid under-segmentation, though the initial surface is far from the target boundary, as shown in Fig.12(p). 3) The proposed method can integrate boundary constraints. In most of applications, the wights of inter-column and intra-column were set to infinity, which makes it difficult to utilize shape $prior$. When the search bound has more strong edge responses, the strong boundary may be detected by using graph search, as shown in Fig.12(k)(the green arrow). However, the proposed method can detect the surface of the liver correctly.

Although encouraging results have been achieved, segmentation accuracy needs to be improved (see Table II and Table III). As can be seen in Fig.11, a large surface distance often occurred in the connection of the liver and vessels. It is important to take into account more special characteristics of the liver's anatomical structure. Therefore, larger training data sets need to be collected to learn more shape variability and preserve shape deformation.

IX. ACKNOWLEDGEMENTS

REFERENCES

[1] J. Ferlay, I. Soerjomataram, M. Ervik, R. Dikshit, S. Eser, C. Mathers, M. Rebelo, D. Parkin, D. Forman, and F. Bray, "Globocan 2012 v1. 0," *Cancer incidence and mortality worldwide: IARC CancerBase*, no. 11, 2013.

[2] O. Ecabert, J. Peters, H. Schramm, C. Lorenz, J. von Berg, M. J. Walker, M. Vembar, M. E. Olszewski, K. Subramanyan, G. Lavi *et al.*, "Automatic model-based segmentation of the heart in ct images," *Medical Imaging, IEEE Transactions on*, vol. 27, no. 9, pp. 1189–1201, 2008.

[3] T. Heimann and H.-P. Meinzer, "Statistical shape models for 3d medical image segmentation: a review," *Medical image analysis*, vol. 13, no. 4, pp. 543–563, 2009.

[4] G. Wang, S. Zhang, F. Li, and L. Gu, "A new segmentation framework based on sparse shape composition in liver surgery planning system," *Medical physics*, vol. 40, no. 5, p. 051913, 2013.

[5] Y. Y. Boykov and M.-P. Jolly, "Interactive graph cuts for optimal boundary & region segmentation of objects in nd images," in *Computer Vision, 2001. ICCV 2001. Proceedings. Eighth IEEE International Conference on*, vol. 1. IEEE, 2001, pp. 105–112.

[6] Y. Boykov and V. Kolmogorov, "An experimental comparison of min-cut/max-flow algorithms for energy minimization in vision," *Pattern Analysis and Machine Intelligence, IEEE Transactions on*, vol. 26, no. 9, pp. 1124–1137, 2004.

[7] Y. Boykov and G. Funka-Lea, "Graph cuts and efficient nd image segmentation," *International journal of computer vision*, vol. 70, no. 2, pp. 109–131, 2006.

[8] P. Campadelli, E. Casiraghi, and A. Esposito, "Liver segmentation from computed tomography scans: A survey and a new algorithm," *Artificial Intelligence in Medicine*, vol. 45, no. 2, pp. 185–196, 2009.

[9] X. Zhou, T. Kitagawa, T. Hara, H. Fujita, X. Zhang, R. Yokoyama, H. Kondo, M. Kanematsu, and H. Hoshi, "Constructing a probabilistic model for automated liver region segmentation using non-contrast x-ray torso ct images," in *Medical Image Computing and Computer-Assisted Intervention–MICCAI 2006*. Springer, 2006, pp. 856–863.

[10] E. van Rikxoort, Y. Arzhaeva, and B. van Ginneken, "Automatic segmentation of the liver in computed tomography scans with voxel classification and atlas matching," in *Proceedings of the MICCAI Workshop 3-D Segmentation Clinic: A Grand Challenge*. Citeseer, 2007, pp. 101–108.

[11] L. Rusko, G. Bekes, G. Nemeth, and M. Fidrich, "Fully automatic liver segmentation for contrast-enhanced ct images," *MICCAI Wshp. 3D Segmentation in the Clinic: A Grand Challenge*, vol. 2, no. 7, 2007.

[12] A. H. Foruzan, R. A. Zoroofi, M. Hori, and Y. Sato, "Liver segmentation by intensity analysis and anatomical information in multi-slice ct images," *International journal of computer assisted radiology and surgery*, vol. 4, no. 3, pp. 287–297, 2009.

[13] R. Pohle and K. D. Toennies, "A new approach for model-based adaptive region growing in medical image analysis," in *Computer Analysis of Images and Patterns*. Springer, 2001, pp. 238–246.

[14] Y. Chen, Z. Wang, W. Zhao, and X. Yang, "Liver segmentation from ct images based on region growing method," in *Bioinformatics and Biomedical Engineering, 2009. ICBBE 2009. 3rd International Conference on*. IEEE, 2009, pp. 1–4.

[15] T. F. Cootes, A. Hill, C. J. Taylor, and J. Haslam, "The use of active shape models for locating structures in medical images," in *Information Processing in Medical Imaging*. Springer, 1993, pp. 33–47.

[16] H. Lamecker, T. Lange, and M. Seebass, *Segmentation of the liver using a 3D statistical shape model*. Citeseer, 2004.

[17] D. Kainmüller, T. Lange, and H. Lamecker, "Shape constrained automatic segmentation of the liver based on a heuristic intensity model," in *Proc. MICCAI Workshop 3D Segmentation in the Clinic: A Grand Challenge*, 2007, pp. 109–116.

[18] X. Zhang, J. Tian, K. Deng, Y. Wu, and X. Li, "Automatic liver segmentation using a statistical shape model with optimal surface detection," *IEEE Transactions on Biomedical Engineering*, vol. 57, no. 10, p. 2622, 2010.

[19] K. Li, X. Wu, D. Z. Chen, and M. Sonka, "Optimal surface segmentation in volumetric images-a graph-theoretic approach," *Pattern Analysis and Machine Intelligence, IEEE Transactions on*, vol. 28, no. 1, pp. 119–134, 2006.

[20] G. Wang, S. Zhang, H. Xie, D. N. Metaxas, and L. Gu, "A homotopy-based sparse representation for fast and accurate shape prior modeling in liver surgical planning," *Medical image analysis*, vol. 19, no. 1, pp. 176–186, 2015.

[21] H. Lombaert, Y. Sun, L. Grady, and C. Xu, "A multilevel banded graph cuts method for fast image segmentation," in *Computer Vision, 2005. ICCV 2005. Tenth IEEE International Conference on*, vol. 1. IEEE, 2005, pp. 259–265.

[22] N. Xu, N. Ahuja, and R. Bansal, "Object segmentation using graph cuts based active contours," *Computer Vision and Image Understanding*, vol. 107, no. 3, pp. 210–224, 2007.

[23] L. Massoptier and S. Casciaro, "Fully automatic liver segmentation through graph-cut technique," in *Engineering in Medicine and Biology Society, 2007. EMBS 2007. 29th Annual International Conference of the IEEE*. IEEE, 2007, pp. 5243–5246.

[24] R. Beichel, A. Bornik, C. Bauer, and E. Sorantin, "Liver segmentation in contrast enhanced ct data using graph cuts and interactive 3d segmentation refinement methods," *Medical physics*, vol. 39, no. 3, pp. 1361–1373, 2012.

[25] M. G. Linguraru, W. J. Richbourg, J. Liu, J. M. Watt, V. Pamulapati, S. Wang, and R. M. Summers, "Tumor burden analysis on computed tomography by automated liver and tumor segmentation," *Medical Imaging, IEEE Transactions on*, vol. 31, no. 10, pp. 1965–1976, 2012.

[26] X. Chen, J. K. Udupa, U. Bagci, Y. Zhuge, and J. Yao, "Medical image segmentation by combining graph cuts and oriented active appearance models," *Image Processing, IEEE Transactions on*, vol. 21, no. 4, pp. 2035–2046, 2012.

[27] H. Song, Q. Zhang, and S. Wang, "Liver segmentation based on skfcm and improved growcut for ct images," in *Bioinformatics and Biomedicine (BIBM), 2014 IEEE International Conference on*. IEEE, 2014, pp. 331–334.

[28] S. Tomoshige, E. Oost, A. Shimizu, H. Watanabe, and S. Nawano, "A conditional statistical shape model with integrated error estimation of the conditions; application to liver segmentation in non-contrast ct images," *Medical image analysis*, vol. 18, no. 1, pp. 130–143, 2014.

[29] X. Chen, M. Niemeijer, L. Zhang, K. Lee, M. D. Abràmoff, and M. Sonka, "Three-dimensional segmentation of fluid-associated abnormalities in retinal oct: probability constrained graph-search-graph-cut," *Medical Imaging, IEEE Transactions on*, vol. 31, no. 8, pp. 1521–1531, 2012.

[30] F. Shi, X. Chen, H. Zhao, W. Zhu, D. Xiang, E. Gao, M. Sonka, and H. Chen, "Automated 3-d retinal layer segmentation of macular optical coherence tomography images with serous pigment epithelial detachments," 2014.

[31] R. T. Whitaker and X. Xue, "Variable-conductance, level-set curvature for image denoising," in *Image Processing, 2001. Proceedings. 2001 International Conference on*, vol. 3. IEEE, 2001, pp. 142–145.

[32] W. E. Lorensen and H. E. Cline, "Marching cubes: A high resolution 3d surface construction algorithm," in *ACM siggraph computer graphics*, vol. 21, no. 4. ACM, 1987, pp. 163–169.

[33] H. Hoppe, "New quadric metric for simplifying meshes with appearance attributes," in *Proceedings of the conference on Visualization'99: celebrating ten years*. IEEE Computer Society Press, 1999, pp. 59–66.

[34] T. Heimann, I. Oguz, I. Wolf, M. Styner, and H.-P. Meinzer, "Implementing the automatic generation of 3d statistical shape models with itk," in *The Insight JournalMICCAI Open Science Workshop, Copenhagen*. Citeseer, 2006.

[35] B. K. Horn, "Closed-form solution of absolute orientation using unit quaternions," *JOSA A*, vol. 4, no. 4, pp. 629–642, 1987.

[36] A. Meijster, J. B. T. M. Roerdink, and W. H. Hesselink, "A general algorithm for computing distance transforms in linear time," in *Mathematical Morphology and its Applications to Image and Signal Processing*, Kluwer Acad. Publ., 2000, pp. 331–340.

[37] X. Chen, J. K. Udupa, A. Alavi, and D. A. Torigian, "Gc-asm: Synergistic integration of graph-cut and active shape model strategies for medical image segmentation," *Computer Vision And Image Understanding*, vol. 117, no. 5, pp. 513–524, 2013.

[38] D. Xiang, J. Tian, F. Yang, Q. Yang, X. Zhang, Q. Li, and X. Liu, "Skeleton cuts - an efficient segmentation method for volume rendering," *Visualization and Computer Graphics, IEEE Transactions on*, vol. 17, no. 9, pp. 1295–1306, 2011.

[39] D. Zorin, P. Schröder, and W. Sweldens, "Interpolating subdivision for meshes with arbitrary topology," in *Proceedings of the 23rd annual conference on computer graphics and interactive techniques*. ACM, 1996, pp. 189–192.

[40] L. R. Herrmann, "Laplacian-isoparametric grid generation scheme," *Journal of the Engineering Mechanics Division*, vol. 102, no. 5, pp. 749–907, 1976.

[41] T. Heimann, B. Van Ginneken, M. A. Styner, Y. Arzhaeva, V. Aurich, C. Bauer, A. Beck, C. Becker, R. Beichel, G. Bekes *et al.*, "Comparison and evaluation of methods for liver segmentation from ct datasets," *Medical Imaging, IEEE Transactions on*, vol. 28, no. 8, pp. 1251–1265, 2009.

[42] A. Wimmer, G. Soza, and J. Hornegger, "A generic probabilistic active shape model for organ segmentation," in *Medical Image Computing and Computer-Assisted Intervention–MICCAI 2009*. Springer, 2009, pp. 26–33.

[43] M. G. Linguraru, W. J. Richbourg, J. M. Watt, V. Pamulapati, and R. M. Summers, "Liver and tumor segmentation and analysis from ct of diseased patients via a generic affine invariant shape parameterization and graph cuts," in *Abdominal Imaging. Computational and Clinical Applications*. Springer, 2012, pp. 198–206.

[44] F. Chung and H. Delingette, "Regional appearance modeling based on the clustering of intensity profiles," *Computer Vision and Image Understanding*, vol. 117, no. 6, pp. 705–717, 2013.

[45] M. Kirschner, "The probabilistic active shape model: From model construction to flexible medical image segmentation," Ph.D. dissertation, Citeseer, 2013.

[46] M. Erdt, S. Steger, M. Kirschner, and S. Wesarg, "Fast automatic liver segmentation combining learned shape priors with observed shape deviation," in *Computer-Based Medical Systems (CBMS), 2010 IEEE 23rd International Symposium on*. IEEE, 2010, pp. 249–254.

Guodong Li received the B.E. degree in Dalian University of Technology, Dalian, China, in 2010. He is currently a Ph.D. candidate in the Key Laboratory of Molecular Imaging, Institute of Automation, Chinese Academy of Sciences, Beijing, China. His current research interests include medical data segmentation, medical image analysis, and pattern recognition.

Jie Tian (M'02−SM'06−F'10) received the Ph.D. degree (with honors) in artificial intelligence from the Institute of Automation, Chinese Academy of Sciences, Beijing, China, in 1992. From 1995 to 1996, he was a Postdoctoral Fellow at the Medical Image Processing Group, University of Pennsylvania, Philadelphia. Since 1997, he has been a Professor at the Institute of Automation, Chinese Academy of Sciences, where he has been the director of Key Laboratory of Molecular Imaging. His research interests include the medical image process and analysis and pattern recognition. Dr. Tian is an IEEE fellow, IAMBE fellow, SPIE fellow, AIMBE fellow.

Xinjian Chen received the Ph.D. degree from the Center for Biometrics and Security Research, Key Laboratory of Complex Systems and Intelligence Science, Institute of Automation, Chinese Academy of Sciences, Beijing, China, in 2006. After completing the graduation, he joined Microsoft Research Asia where he was involved in research on handwriting recognition. From January 2008 to May 2012, he has conducted the Postdoctoral Research at several prestigious groups: Medical Image Processing Group, University of Pennsylvania; Department of Radiology and Image Sciences, National Institutes of Health; Department of Electrical and Computer Engineering, University of Iowa. On June 2012, he joined the School of Electrical and Information Engineering, Soochow University, as a Full Professor. His research interests include medical image processing and analysis, pattern recognition, machine learning, and their applications. Up to now, he has published more than 70 high quality international journal/conference papers. He is now a Distinguished Professor at Soochow University, and serve as Director of a University level lab- Medical Image Processing, Analysis and Visualization Lab.

Dehui Xiang received the B.E. degree in automation from Sichuan University, Sichuan, China, in 2007, and received the Ph.D. at the Institute of Automation, Chinese Academy of Sciences, Beijing, China, in 2012. Now he is a associate professor at School of Electronics and Information Engineering, Soochow University, Jiangsu 215006, China. His current research interests include medical image analysis, computer vision, medical data visualization, and pattern recognition.

Fei Shi received the B.E. degree in Information and Electronics Engineering from Zhejiang University, Hangzhou, China, in 2002, and received the Ph.D. in Electrical Engineering from Polytechnic University, New York, USA, in 2006. Now she is an assistant professor at School of Electronics and Information Engineering, Soochow University, Suzhou, China. Her current research interests include medical image analysis and pattern recognition.

Weifang Zhu received the B.E. and M.S. degree from Xi'an Jiaotong University, Shanxi, China, in 2000 and 2003, respectively, and received the Ph.D. from Soochow University, Jiangsu, China, in 2013. Now she is an associate professor at School of Electronics and Information Engineering, Soochow University, China. Her current research interests include medical image analysis, machine learning and pattern recognition.